Outdoor performance of a tandem InGaP/Si photovoltaic luminescent solar concentrator

Megan Phelan [a],[1], David R. Needell [a],[1], Haley Bauser [a],[1], Hanxiao Su [b], Michael Deceglie [c], San Theingi [c], Brent Koscher [d], Zach Nett [d], Colton R. Bukowsky [a], Ognjen Ilic [a], Paul Stradins [c], John Geisz [c], Ralph Nuzzo [b], A. Paul Alivisatos [d],[e], Harry A. Atwater [a],[*]

[a] California Institute of Technology, Department of Applied Physics and Materials Science, CA, 91125, USA
[b] University of Illinois and Urbana-Champaign, Department of Chemistry, IL, 61801, USA
[c] National Renewable Energy Laboratory, CO, 80401, USA
[d] University of California Berkeley, Department of Chemistry, CA, 94720, USA
[e] Lawrence Berkeley National Laboratory, CA, 94720, USA

ARTICLE INFO

ABSTRACT

We report the design, fabrication and outdoor characterization of a tandem luminescent solar concentrator/Si multi-junction photovoltaic module. Our tandem LSC/Si device consists of an InGaP LSC functioning as a top cell and a passivated contact Si bottom cell. The LSC comprises of an InGaP microcell array coupled to a polymer waveguide, loaded with CdSe/CdS core-shell quantum dot luminophores. The light trapping efficiency of the LSC waveguide is enhanced by encapsulation with photoluminescence trapping mirrors consisting of dielectric multilayer thin films. We demonstrate the performance of the LSC/Si device through a series of outdoor tests under various irradiance conditions conducted at the National Renewable Energy Laboratory. We report the first outdoor testing data of an LSC/Si tandem module, displaying maintained performance across varied diffusivity conditions for the LSC component. Finally, we model the tandem module performance using a ray optic simulation-based multiphysics model and forecast a pathway for high efficiency tandem LSC/Si module performance.

1. Introduction

Traditional flat plate photovoltaic (PV) devices often exhibit inconstant power conversion under varied illumination conditions. For instance, operation under diffuse lighting conditions can lead to a 20% reduction in power conversion efficiency (PCE) for monocrystalline silicon cells relative to direct solar irradiance [1,2]. Moreover, standard solar radiation data compiled across the United States suggests that diffuse irradiance can compose between 20 and 40% of the global radiation, depending upon geographical region and time of year [3,4]. Solar technologies equipped with diffuse-light capture mechanisms stand to further increase adoption of PV systems.

Considerable research is currently being directed toward developing scalable, thin-film tandem or tandem-on-silicon PV cells and modules, which have potential for efficiencies beyond the practical and theoretical limits [5] of single-junction devices by utilizing a larger portion of the solar spectrum [6]. Currently, the highest efficiency stabilized thin-film tandem PV performance has been achieved using III-V compound semiconductor tandems, with the highest efficiency devices composed of III-V materials grown on silicon [7]. However, at present, the costs for III-V materials in thin-film or silicon tandem device configurations is too high to be economical for large-scale applications [8]. Other pathways for tandem PV devices are being actively explored. Among these, notable high efficiency lead halide perovskite on silicon tandem prototypes have been reported, although the long-term stability of these tandem devices is, as of today, unproven [9].

An alternative approach to high efficiency tandem modules with potential to reduce the overall module cost of III-V/Si tandems is to concentrate incident sunlight onto an array of small III-V micro-cells, thereby minimizing the amount of III-V material required per watt of generated electricity [10,11]. Uniquely among PV concentrators, luminescent solar concentrators (LSCs) enable concentration of both diffuse

---

and direct light [10,12]. LSCs can also be developed in flat-plate, fixed-axis modules that do not require sun tracking, enabling such technology to be particularly suitable to applications of conventional, single-junction PV modules. In an LSC, light is concentrated from a waveguide absorption area, A, to a solar cell collection area, A'; this ratio of concentration areas is referred to as the geometric gain, where G = A/A' [10]. Functionally, the absorbed incident sunlight is trapped within a dielectric waveguide through total internal reflection (TIR). The trapped light is then redirected to small area PV cells for energy conversion. LSCs employ luminophores uniformly dispersed within the waveguide that isotropically absorb high energy photons and re-radiate down-converted photons as photoluminescence (PL) with a high radiative efficiency, or photoluminescence quantum yield (PLQY). For an ideal LSC with a perfect light trapping waveguide, the concentration equals the geometric gain (C = G); however, waveguide nonidealities result in C < G [10]. Initial studies demonstrate the ability of stand-alone LSCs to capture both direct and diffuse irradiance, allowing sustained performance in varied lighting conditions [13–15]. The concentration of luminophores dispersed within the waveguide determines the amount of irradiance absorbed, quantified as a spectrally dependent optical density. Ideal luminophores require a large Stokes shift—the downshift between absorbed and emitted photon energies—in order to reduce reabsorption losses [16]. PL radiation is trapped within the waveguide as a result of coupling into guided optical modes, arising from TIR. Since TIR traps only a portion of the PL, LSCs often employ additional external reflectors enclosing the top and bottom surfaces of the waveguide [17–19].

While the performance of single-junction cells has been evaluated under diffuse irradiance conditions using many optical configurations (conventional texture-etched Si cells [20], dielectric nanosphere arrays [21], plasmon nanostructures [22–24], and light trapping wire arrays [25,26]), device performance of tandem LSCs, has not been studied for varied irradiance conditions. Here we investigate designs for III-V/Si LSC devices that combine arrays of micro-processed InGaP cells embedded within an LSC and optically integrated with a flat plate Si cell for use as a four terminal tandem module. For an optically efficient LSC, the concentration factor can approach the geometrical gain (GG), defined to be the ratio between the total device illuminated surface area and the area of the III-V PV material. If high concentration factors (>30x) can be achieved, this tandem LSC/Si approach has the potential to increase module efficiencies beyond 30%, well beyond current single-junction performance limits, while dramatically reducing the cost per watt of the utilized III-V material [11,19].

Tandem LSC/Si modules address all critical requirements for tandem PV technology implementation: *i)* functionality in both direct and diffuse lighting conditions, *ii)* efficient solar spectrum utilization via a multi-junction module, and *iii)* reduced materials cost due to integration with silicon and the small area fraction for the III-V material (i.e., high GG). In this study, we analyze the first-ever fabricated LSC/Si tandem module, as shown schematically in Fig. 1. The module consists of (from the top-down): *i)* a top dielectric aperiodic stack notch filter, *ii)* a polymeric LSC waveguide of poly(lauryl methacrylate) (PLMA) with uniformly dispersed CdSe/CdS core/shell quantum dots (QDs), *iii)* an InGaP III-V micro-cell array, *iv)* a bottom dielectric aperiodic stack notch filter, and *v)* a passivated contact Si subcell. Finally, we supply specular reflective acrylic-Al mirrors along each of the module edges to reduce photon losses from edge out-coupling.

Fig. 1 shows both photographic (Fig. 1a and b) and rendered schematics (Fig. 1c) of the LSC/Si tandem module. Fig. 1d displays a conceptual schematic of the core/shell structure of the CdSe/CdS QDs, as well as a transmission electron microscope (TEM) image of the nanoparticles. To convert PL (Fig. 1a) into electrical power, we fabricate a micro-cell array, composed of embedded III-V InGaP cells with active areas of 400 μm × 400 μm per cell, shown in the optical microscope image in Fig. 1e. We set this array in tandem with a passivated contact silicon subcell optimized to harvest long-wavelength photons. Though the embedded InGaP micro-cell planar array occupies a small area fraction, it acts as a PL sink, concentrating QD emitted light to the micro-cells. Previous studies have shown the concentration mechanism for analogous, single solar cell LSC structures [27–30]. The long wavelength portion of incident light spectrum not converted into PL is thereby transmitted to the Si cell. By optically coupling the LSC component to the InGaP micro-cell array and matching the PL of the QD luminophores to the InGaP energy bandgap, we concentrate sunlight irradiance in the ultraviolet/blue part of the spectrum onto high radiative efficiency InGaP micro-cells to enable higher module efficiency. Our fabricated module is a four terminal structure, reducing the risk of J_{SC} mismatch and series resistance between the top LSC and bottom Si. Fig. 1b shows the realized LSC-InGaP microcell array that is placed atop the silicon subcell. The PL of the QD-waveguide under UV-light is shown in Fig. 1a.
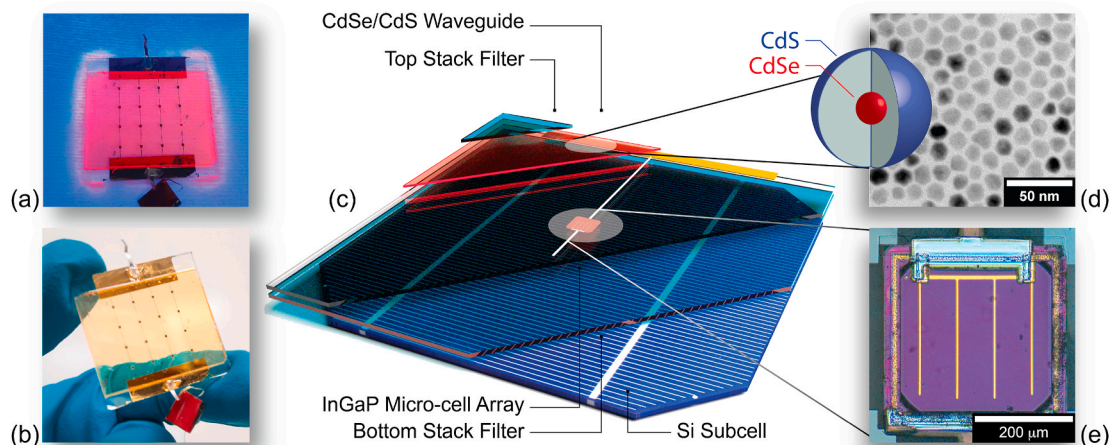

Fig. 1. The tandem LSC/Si, four terminal module. (a) The top LSC component consisting of a 4 × 4 InGaP micro-cell array encapsulated within a 30 μm (μm) thick CdSe/CdS core/shell QD waveguide under UV illumination, visibly displaying PL in the red. (b) The same top LSC component as (a), under ambient light held for scale. We note that, as viewed in (a) and (b), the right-most column of InGaP micro-cells (4 cells in total) electrically shorted during fabrication process, yielding an effective 4 × 3 micro-cell array. (c) A 3D rendering of the full tandem LSC/Si module with PL trapping stack filters coupled to the top and bottom surfaces of the LSC waveguide/InGaP micro-cell array component. (d) The core/shell structure of the CdSe/Cds QDs alongside a transmission electron microscope (TEM) image. (e) A confocal microscope image of the anchored InGaP micro-cell on the LSC glass substrate, with cell dimensions of approximately 400 μm x 400 μm. (For interpretation of the references to colour in this figure legend, the reader is referred to the Web version of this article.)

Fig. 2a and b shows the measured, spectral characteristics for the LSC and Si components of the tandem module. The full AM1.5G spectrum impinges upon the top surface of the LSC device. CdSe/CdS QDs absorb photons in 400–500 nm wavelength range and photoluminesce at a peak wavelength of 635 nm, spectrally matching the InGaP electronic bandgap (Fig. 2a). This PL is trapped within the waveguide by both TIR and top/bottom notch filters, which reflect photons centered around the QD PL (Fig. 2a). Incident photons not absorbed by the QDs or reflected by the notch filters pass through the LSC to the Si subcell. Given the high external quantum efficiency (EQE) for the passivated contact Si cell at longer wavelengths (Fig. 2b), this design actively splits the incident spectrum between high energy photons (LSC) and low energy photons (passivated contact Si). As shown in Fig. 2b, the transmitted light incident on the Si subcell is a truncated AM1.5G spectrum due to photons that have been either absorbed and trapped by the top LSC component, or reflected by the notch filters. With proper spectral tuning of the notch filters, increased PL collection by the InGaP micro-cells outweighs filter reflection losses [11]. Fig. 2c and d shows the simulated and measured notch filter reflectance, respectively. In this design we use an aperiodic, dielectric layered structure consisting of Ta_2O_5 (high index) and SiO_2 (low index) in order to achieve this notch profile. We observe a close match between simulated and measured transmittance values, with slightly lower transmittance in the high photon energy pass band of the fabricated mirror owing to absorption from the thick, 2 mm glass substrate of the dielectric stack.

We conducted indoor laboratory measurements, taken under one-sun solar simulation, to reveal the optical properties of each component in the module. Fig. 3a and b illustrate the effects of individual LSC components on the EQE performance in an analogous layer-by-layer fashion. As the LSC components shape the incident light spectrum, fewer photons are collected by the Si subcell, as seen in Fig. 3b. Light

current-voltage (LIV) measurements reveal a $J_{SC} = 29.3$ mA/cm^2 and a $V_{OC} = 0.7$ V for the bare Si subcell, and a $J_{SC} = 12.9$ μA/cm^2 and a $V_{OC} = 4.5$V for the 4×3 InGaP micro-cell array under the LSC waveguide. With each layer added to the full device, the total output current from the Si is reduced and V_{OC} decreases slightly (Fig. 3c). Additionally, the 4×3 InGaP array experiences a current drop off with the addition of the top filter (Fig. 3c) as a result of the reduced EQE spectrum of the InGaP micro-cell. However, as discussed later, given proper tuning of the notch filter and LSC parameters (e.g., concentrated QD loading, GG), increased PL trapping will offset the drop-off in the InGaP micro-cell EQE spectrum with the addition of the top filter, thus resulting in an enhanced power output of the full device.

We analyzed the power performance of a fabricated array of 12 InGaP micro-cells—four cells connected in series across three columns in parallel, spaced 4 mm apart—optically coupled to a QD LSC with an overall GG of 250. Of note, the 4×3 microcell array tested corresponds with a sparser design than is optimal, as shown by the high GG, due to fabrication challenges of a fully-dense InGaP cell array; for a denser array with tighter InGaP cell spacing, we would expect a higher photocurrent density of the LSC top component as discussed in the final device modeling section. In order to ensure complete optical coupling, we deposit the LSC QD waveguide directly atop the InGaP micro-cell array. We show here periodic current-voltage (IV) measurements of the LSC/Si tandem module throughout an outdoor field test performed in the week of November 12th, 2018 at the National Renewable Energy Laboratory (NREL) in Golden, CO. In addition, we simulated loss mechanisms intrinsic to this design via a Monte Carlo ray-tracing algorithm. We spatially mapped the PL collection of a single InGaP micro-cell within the QD waveguide to determine photon travel distances within the LSC to further analyze efficiency loss mechanisms. Finally, we designed and optimized the tandem LSC/Si module addressing each
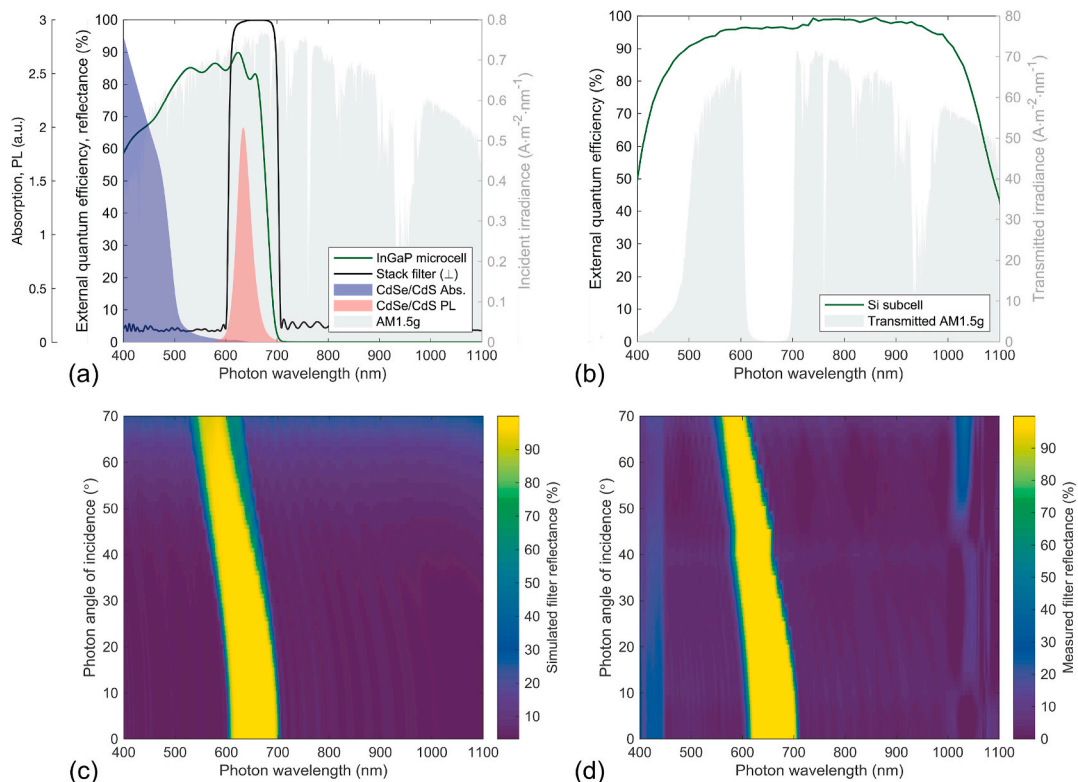

Fig. 2. The spectral characteristics of the tandem LSC/Si module. (a) The top LSC PV component, comparing the spectra of the absorption/PL of the CdSe/CdS QDs (far left y-axis), the external quantum efficiency (EQE) of the anchored InGaP micro-cell (left y-axis), the stack filter reflectance spectrum at normal incidence (left y-axis), and the incident AM1.5G spectrum (right y-axis). (b) The bottom Si component of the tandem LSC/Si module, comparing the spectra of the passivated contact Si cell EQE (left y-axis) against the transmitted irradiance through the LSC component (right y-axis). (c), (d) The simulated and measured dielectric, aperiodic stack filter with alternating layers of Ta_2O_5 and SiO_2, respectively. The realized stack filter (d) is deposited atop an approximately 2 mm thick glass substrate.
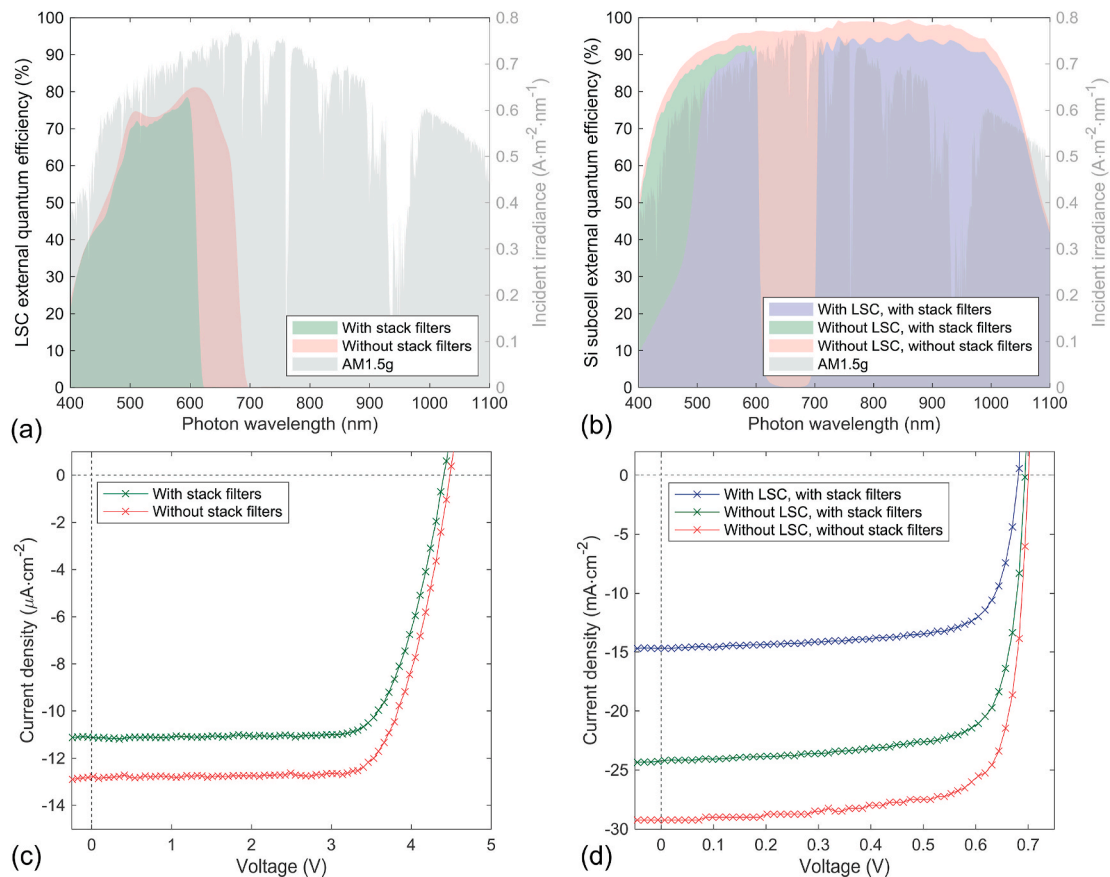
Fig. 3. The measured electrical performance of the tandem LSC/Si device under artificial, AM1.5G light via a solar simulator. (a) The EQE analysis for the top LSC component for the cases with and without PL-trapping stack filters. (b) The EQE analysis for the bottom, passivated contact Si component for the cases with the LSC and PL-trapping stack filters, with only the stack filters, and finally without the LSC or the filters. (c) Light IV measurements of a sparse InGaP micro-cell array top LSC component for the cases with and without PL-trapping stack filters, under AM1.5G illumination. (d) Light IV measurements of the Si passivated contact bottom cell for the same cases as in (b), under AM1.5G illumination.

identified loss mechanism and sources of inefficiency to forecast the performance limits for such tandem module designs.

2. Methods and module fabrication

Upright n-on-p InGaP solar cells were grown on GaAs substrates by atmospheric-pressure metal-organic vapor phase epitaxy (MOVPE) [31, 32]. The Zn-doped absorber layer was approximately 900 nm thick with a 2 μm $Al_{.5}Ga_{.5}As$ lateral conduction layer (LCL) for transparency, which allowed bifacial operation of the device. An AlInP layer was used beneath the LCL as a sacrificial layer for lifting off micro-cells during transfer printing. For the fabrication of micro-cells, the geometry of the n-contact was first defined via photolithography. A contact layer with 10 nm of Ni and 1 μm of Au was then electrodeposited. The cell mesa was defined with a two-step wet etch, the first being a 1:100 bromine-hydrobromic (48% HBr, Sigma-Aldrich) acid etch, to non-selectively complete the main part of the etch; the second being a saturated HCl etch, to selectively remove the remaining InGaP and expose a smooth, undamaged LCL. The p-contact was deposited similarly, and the devices were isolated by another HCl etch, exposing the GaAs substrate. Silicon nitride was deposited over the device via plasma-enhanced chemical vapor deposition (PECVD) to reduce Fresnel losses and non-radiative recombination. Contact windows and lift-off edges were opened via CF_4 reactive ion etch (RIE). A secondary on-cell Au contact was deposited by sputtering. Photoresist was used to anchor the cells for lift off. A 1:4 HCl–H_2O etchant was used to remove the sacrificial layer.

A 150 nm layer of spin-on-glass/epoxy (SOG-E) adhesive [33] was

deposited on top of a soda-lime glass substrate of 2.5 cm × 2.5 cm. A polydimethylsiloxane (PDMS) stamp was then used to transfer the micro-cells, isolated by the RIE etching process, to the glass substrate deterministically to form an array of cells [34,35]. The SOG-E layer was cured by sequential heating and UV exposure. The edges of the cells were insulated with SU-8 2025 to avoid shorting. A Cr/Cu/Al/Au interconnect was then sputtered to complete the array.

To obtain high luminophore spectral performance, we fabricated CdSe/CdS core/shell QDs closely following literature procedures [19]. Absorption spectra were measured using a Shimadzu UV-3600 double beam spectrometer. Measurements were conducted at dilute concentrations to minimize the influence of scattering. PL spectra were measured using a Horiba Jobin-Yvon FluoroLog steady-state spectro-fluorometer, exciting above the bandgap at 430 nm. The detection PMT of the spectrofluorometer was calibrated for spectral sensitivity. For TEM analysis, dilute solutions of the nanocrystal stock solution were drop cast onto TEM grids (Electron Microscopy Sciences CF400–Cu). Multiple TEM images with thousands of quantum dots were sized using an automated analysis script to ensure consistency from the nanoparticle synthesis.

We dispersed core/shell QD particles within the monomers lauryl methacrylate (LMA, Sigma-Aldrich) and ethylene glycol dimethacrylate (EGDMA, Sigma-Aldrich) at a 10:1 ratio. Darocur 1173 (Sigma-Aldrich) photoinitiator was added at 0.05% volume. We placed 30 μm, soda-lime glass spacers atop the 2.5 cm × 2.5 cm glass substrate (hosting the InGaP micro-cell array) and mounted a capping, quartz glass superstrate atop the spacers, treated with repel-silane (GE Healthcare). To obtain a 30 μm waveguide thickness, we applied a capillary force method, injecting the

QD/monomer solution between the glass substrate/InGaP array and the glass superstrate. We cured the QD/monomer solution under 365 nm UV exposure, afterwards the quartz glass superstrate can be removed after curing, as the repel-silane surface treatment prevents strong bonding to the polymer waveguide.

We designed and optimized the dielectric, aperiodic notch filter stack following a previously used optimization procedure [11]. We fabricated the stack filter onto a 2.5 cm × 2.5 cm x 2 mm glass substrate with an anti-reflective coating opposite the dielectric stack (Evaporated Coatings Inc., Willow Grove, PA USA). We mechanically stacked the InGaP array/LSC component directly on the bottom dielectric stack filter and glass substrate. We similarly placed the top dielectric filter atop the PLMA-QD waveguide to complete our device design. Finally, we placed this bottom filter/InGaP micro-cell array/PLMA-QD waveguide/top filter structure atop a passivated contact Si cell with a window area of 1.6 cm × 2.5 cm.

Our bottom Si subcell is a single side textured, rear junction cell with heavily doped n-type and p-type poly-Si/SiO$_x$ passivation layers deposited at the front and the back of an n-type Cz wafer respectively. First, 170 μm thick, single side textured, 2.5–3 Ohm cm n-Cz wafers were cleaned using piranha, standard RCA 1 and RCA 2 process. Then, approximately 1.5 nm thick low temperature thermal tunneling SiO$_x$ was grown on an RCA cleaned single side textured n-Cz wafer. A 50 nm thick PECVD grown n-type and p-type doped hydrogenated amorphous silicon (a-Si:H) was then deposited on top of this tunneling oxide. The sample was placed inside a diffusion furnace in an N$_2$ environment at 850C for 30 min to simultaneously diffuse the dopants and crystallize amorphous Si to polycrystalline Si. 15 nm of alumina oxide is then added using atomic layer deposition and is activated at 400C in a forming gas environment to enhance the passivation. The resulting cell has a passivation that can reach above 730 mV in iV$_{oc}$ and ~10 fA/cm^2 J$_0$ values. The metal contacts were formed by thermally evaporating titanium and silver through the openings of a shadow mask. We soldered metal ribbons to the pads at the end of the busbar and the back contact to provide electrical leads for the tandem configuration [36].

The passivated contact Si cell was measured using a solar simulator under 1 sun condition and then measured again under the CdSe/CdS waveguide and bottom filter stack to estimate the performance of the cell in the LSC/Si configuration. Under 1 sun, the cell achieves V$_{oc}$ of 703.2 mV, J$_{sc}$ 38.9 mA/cm^2, and an efficiency of 20.6%. When this cell is measured under the waveguide and the filter stack, the V$_{oc}$ of the cell decreases to 694 mV, and J$_{sc}$ to 27.3 mA/cm^2 due to the reduced incident illumination on the cell, resulting in an efficiency of 14.4% for Si subcell. We encapsulate this Si subcell with a mm-thick layer of Polydimethylsiloxane (PDMS). In order to approximate a large-area III-V micro-cell array via side loss reduction, we place this tandem LSC/Si device within a mirrored acrylic test bed [37]. We measure the reflectance of this rectangular trench with a Varian Cary 5G UV–Vis spectrophotometer.

We apply a Monte Carlo, ray-tracing model to stochastically simulate the performance (photocurrent, J$_{sc}$) of this four terminal, tandem LSC/Si device. We initialize greater than 2×10^6 individual photons to strike the top surface of the tandem module, spectrally distributed between the wavelengths of 300–1500 nm, and spatially segmented given a mesh grid of 25 μm over the top surface area. We trace each photon throughout the device, keeping track of the current and previous positions, current and past wavelengths, current and past photon velocity vectors, and photon polarization. We apply the Beer-Lambert law given the QD concentration within the PLMA waveguide (via the measured optical density) to determine the probability of photon absorption via dispersed luminophores for a given photon step. We apply Snell and Fresnel laws to determine the trajectory of each photon upon change of refractive index and material interaction. We apply the measured transmittance and reflectance of the top/bottom PL filters with respect to wavelength and angle of incidence within the model to determine the interaction of photons with these layers. Finally, we implement the

reflectance and internal quantum efficiency of both the silicon subcell and InGaP micro-cell to determine the amount of generated photocurrent within each cell type. All photons simulated terminate in either collection by one of the two cell types or termination by one of the loss mechanisms, as discussed in Fig. 6. All details regarding the algorithm, implementation, and model validation to experimental studies can be found in previous studies by Needell et al. [38] and Bronstein et al. [27].

3. Outdoor testing results

We determined the effects of irradiance and diffuse light illumination on tandem LSC/Si performance through outdoor field testing, with modules tilted at a fixed 40° relative to horizontal with continuous on-site irradiance measurements [39]. We found that power output as a function of the time-of-day (Fig. 4a and b) achieves its maximum performance near 12:00 p.m. As seen in Fig. 4a and b, this maximum power for both components coincides with maximum solar irradiance (Fig. 4c) as well as an angle of incidence nearest to normal incidence of the module (Fig. 4d) given the tilted axis of the field-test. The supporting information details the direct affect of angle of incidence on both LSC and Si subcell device power output. By 4:00 p.m. and onwards, limited incident irradiance and large off-normal angle of incidence results in negligible output power of the module. We observe similar temporal trends for both the Si subcell and the LSC top cell. Shown in Fig. 4a, the maximum power output decreases across the LSC over the course of the three testing days, a trend not seen in the Si subcell power output vs. time-of-day (Fig. 4b). Such a power decrease implies a degradation mechanism of the LSC component itself, most likely attributed to photodegradation of the PLQY of the luminophores [40,41].

One of the most promising features of such an active concentrator LSC design results from the sustained functionality in both direct and diffuse illumination conditions. Shown in Fig. 5a, we demonstrated outdoor field testing data that is consistent with the PCE trends found in previous work for LSCs [13] as well as for simulated tandem LSC/Si devices operating under varied diffuse and direct irradiance conditions [11]. Seen in Fig. 5b, the Si subcell power conversion efficiency begins to monotonically decrease once the amount of DNI light drops below 50 mW/cm^2. In contrast, the top LSC component does not demonstrate a steady decreasing trend in PCE as a function of DNI. Of note, the slight spread in normalized efficiency for both the LSC and Si components in Fig. 5b is due to discrete trends associated with each day's data collection. These spreads may be a result of the day-to-day variations in testing conditions. Moreover, we hypothesize that the slight drop in normalized efficiency for the Si subcell towards maximum DNI * Irradiance of 100, which typically occurs near noon, may result from the change of the solar spectrum after noon. Fernandez et al. have shown that higher angles of incidence, as occur in the afternoon, produce a larger attenuation of the UV–visible region of the spectrum, resulting in a red-shifted spectrum [42]. A red-shifted solar spectrum is better matched to the silicon band edge, potentially leading to a slight increase in performance, as seen in Fig. 5b.

4. Device performance analysis

Our device underperforms previous simulated work of an LSC/Si tandem design, which suggests an optimized LSC/Si tandem module can reach power conversion efficiencies near 29% [11]. In this study, the Si subcell—when integrated in the LSC/Si tandem module—performed at a 10% PCE, and the LSC component contributed 0.04% PCE. To identify loss mechanisms and optimize our design performance, we simulated the LSC/Si tandem module design with a Monte Carlo ray-tracing algorithm and detailed balance model in order to observe how experimental data match with model predictions. Previous work shows this model to be in strong agreement with experimental observation [38]. We applied this computational tool to understand the causes of lowered output current by the top LSC component. Fig. 6 illustrates the primary
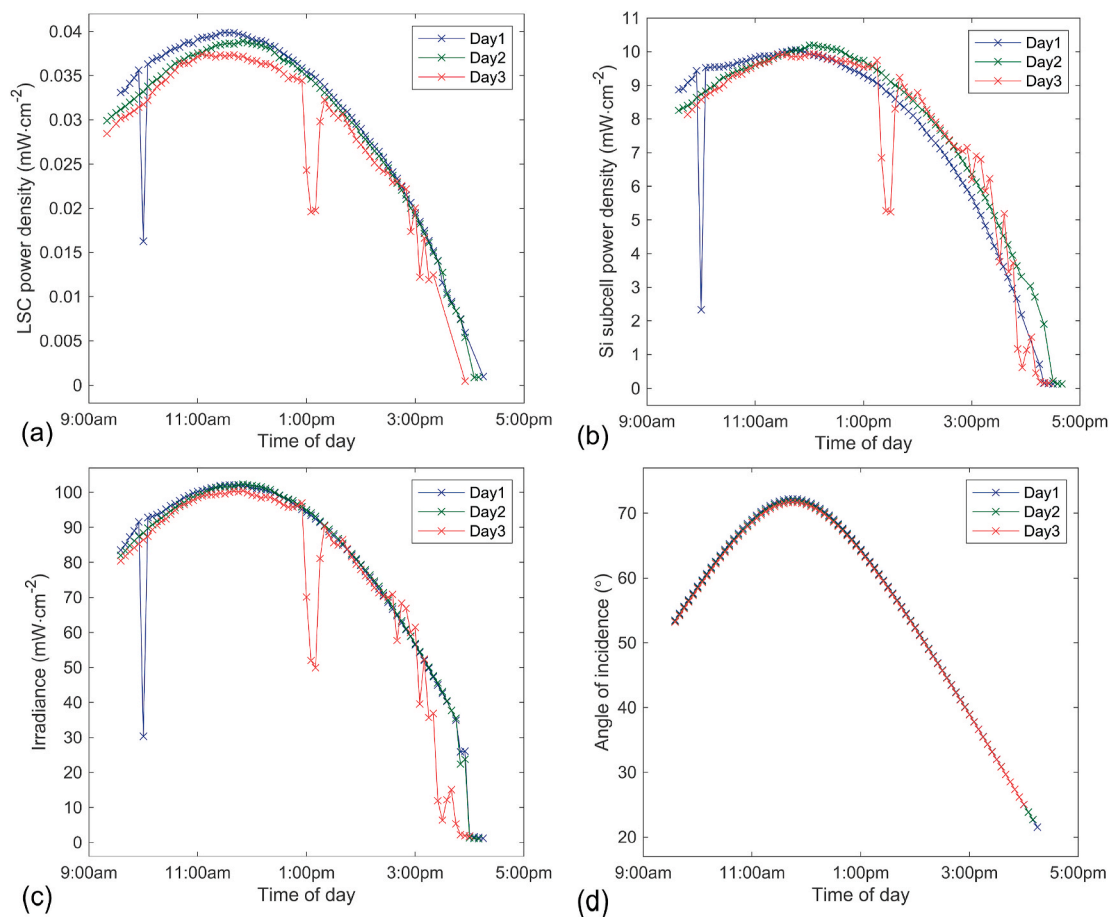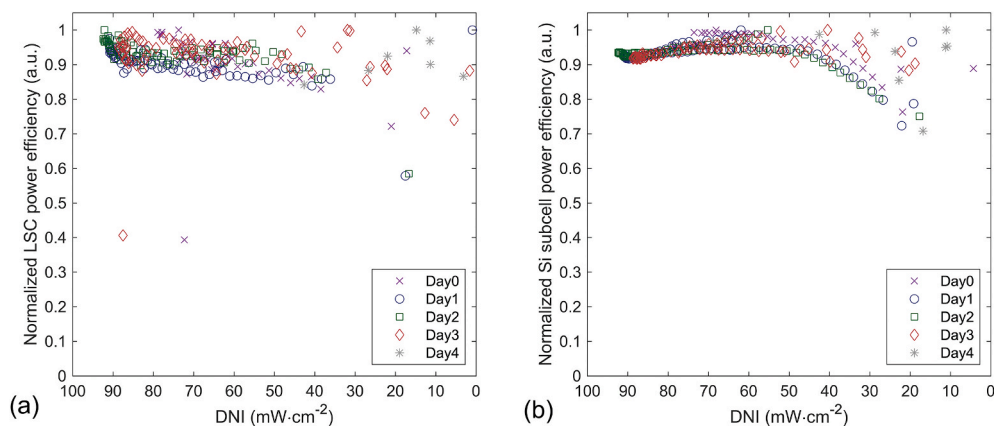
Fig. 4. Outdoor testing results with respect to time of day at the National Renewable Energy laboratory in Colorado, USA for November 13th, 14th, and 15th 2019. (a) The top LSC component and (b) the bottom Si cell component power output in mW per cm² over the course of three full days of testing. (c) The solar irradiance (mW per cm²) and (d) angle of incidence (AoI) (degrees) relative to the modules' top surface for each day of testing, where 90 degrees signifies normal incidence. Dips in the data correspond to brief periods of cloud and/or snow coverage at the testing facility.

Fig. 5. Outdoor testing results with respect to direct normal irradiance (DNI) at the National Renewable Energy laboratory in Colorado, USA for November 12th (partial day), 13th, 14th, 15th, and 16th 2019. Here we show the normalized efficiency for the (a) top LSC component and (b) bottom Si component. We normalize each individual day's power conversion efficiency to the highest efficiency for that given day. Days 3 and 4 of (a) correspond to the case with no top PL-trapping stack filter.

loss mechanisms that limit the performance of such a tandem structure. We found the most significant areas of photon loss stem directly from: *i)* top filter reflection of incident irradiance, *ii)* non-radiative recombination of absorbed photons by the QD luminophores (i.e., non-unity PLQY), *iii)* scattered photons lost through the escape cone of the waveguide/filter component, and *iv)* parasitic Si subcell absorption (e. g., incomplete light coupling into the wafer by the front texture and antireflective coating (ARC), absorption of the trapped near infrared (NIR) light by the back reflector). We illustrate such loss mechanisms

schematically and spectrally in Fig. 6a and b, respectively.

In the short wavelength regime (wavelengths below the notch filter stop-band), the primary loss mechanism results from non-radiative QD absorption due to non-unity PLQY. From ray-tracing simulations and performance matching to outdoor data, we found QD PLQYs to decrease down to approximately 60% over the course of the testing period. As shown in Fig. 4a, we found that the power output of the LSC degraded steadily over each day, implying potential generation of defects in QDs within the waveguide performance, which we attribute to decreasing
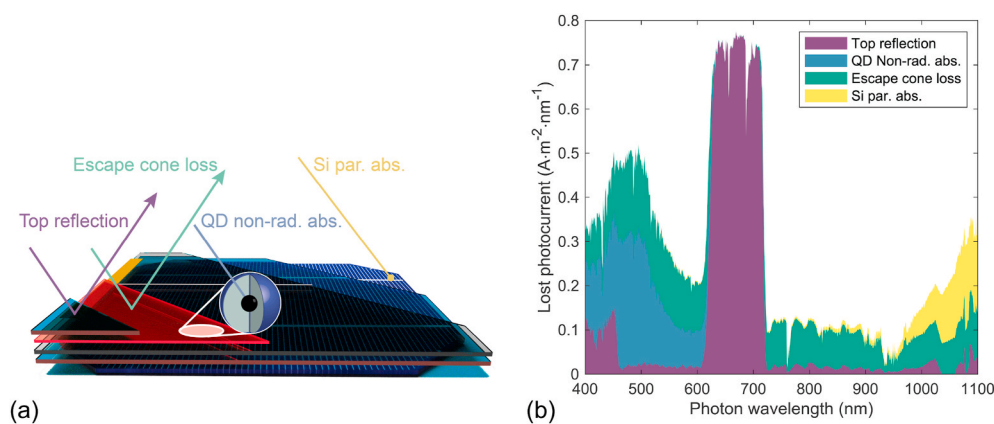
Fig. 6. Computational results showing the primary loss mechanisms responsible for underperformance in the tandem LSC/Si system. (a) A rendered schematic depicting the various loss mechanisms, including: top surface reflection of incident sunlight due, primarily, to the top notch filter (purple), escape cone loss from the LSC waveguide (green), QD non-radiative recombination absorption (blue), and Si parasitic absorption (yellow). (b) The spectral account for the full tandem LSC/Si loss mechanisms, given as the total lost photocurrent (amps per m^2 per nm). (For interpretation of the references to colour in this figure legend, the reader is referred to the Web version of this article.)

QD PLQY. As the LSC PLQY degrades, the probability of photon loss due to QD absorption increases, thereby causing decreased power output.

For wavelengths within the stop-band of the filters, reflection due to this spectral feature is the main cause of photon loss. While the near-perfect reflectance from the notch filter around the 600–700 nm spectral range increases PL trapping and photocurrent delivery to the InGaP micro-cells within the LSC waveguide, it also prevents photons within this frequency range to be transmitted through the top surface to reach either the InGaP array or Si subcell. With near-unity PLQY QDs, PL trapping within the LSC outweighs the reflected incident photon loss within this wavelength range. The finite top-filter reflectance below 500 nm light correspondingly reduces the produced PL. Improved filters could increase spectral transmission down to at least 400 nm and enhance QD photon absorption. Another cause of decreased LSC photocurrent results from PL photon loss through the escape cone of the PLMA waveguide due to top filter transmission. Peak filter reflectivity blue-shifts with angles of incidence as illustrated in Fig. 2c and d. PL that scatters or emits into larger angles of the waveguide escape cone decreasingly reflects back into trapped modes. Finally, a fraction of the low energy photons ($\lambda > 900$ nm) collected by the Si subcell is lost due to parasitic absorption.

As shown in the photocurrent loss mechanisms in Fig. 6b, QD non-radiative absorption and waveguide escape cone re-emission account for a vast portion of loss mechanisms for the LSC component. Improved PL collection requires increased optical efficiency of the waveguide [43]. We spatially mapped the photoluminescence emission within the waveguide by scanning a 490 nm wavelength, 10 μm spot-size beam [44] across an analogous single InGaP micro-cell LSC. We illuminated the waveguide from the corner of the 0.16 mm^2 micro-cell and extend

into a spatial quadrant analyzing a 2.5 cm × 2.5 cm waveguide area—equivalent to a GG of 625—shown in Fig. 7a. As seen, the measured photocurrent drops with the spatial separation between the illumination point and the micro-cell corner. An inflection point in the steep drop off located less than 0.2 mm from the quadrant origin indicates a combination of PL and nearby scattered, short wavelength light collected in this small radius. Such an inflection reveals that the mean photon travel distances within the LSC waveguide are significantly limited by a convolution of escape-cone and non-radiative QD losses.

Via an understanding of the loss mechanisms in the LSC, we can design an improved tandem device. Fig. 7b projects the modeled power conversion efficiency, as well as the associated photocurrents for each the LSC top component and Si subcell, possible for various approaches to component optimization for the tandem LSC device under ideal conditions (e.g., normal incidence sunlight). One promising method for maintaining QD stability and enhancing PLQY performance involves the use of siloxane as a part of the waveguide matrix, which has shown to help QDs maintain PLQY across high temperature and various moistures due to the strong thermal stability of the bonds in the siloxane [45]. In Fig. 7b, we model the following optimizations: *i)* unity PLQY, improved from the current modeled conditions of 60%, *ii)* a defect free waveguide, consisting of an increased quality factor of the QDs, defined as the ratio of absorption at the band edges of CdSe to CdS [46], and non-aggregated dispersion of luminophores within the polymer [47]; *iii)* minimized PL leakage from the device edges; *iv)* optimized top/bottom filters to reduce loss from low-wavelength incident photon reflection and scattered photon transmission through the waveguide escape cone; *v)* a decreased geometric gain (from 250 to 10) of the LSC for higher PL micro-cell collection yields, without obscuring long-wavelength photons
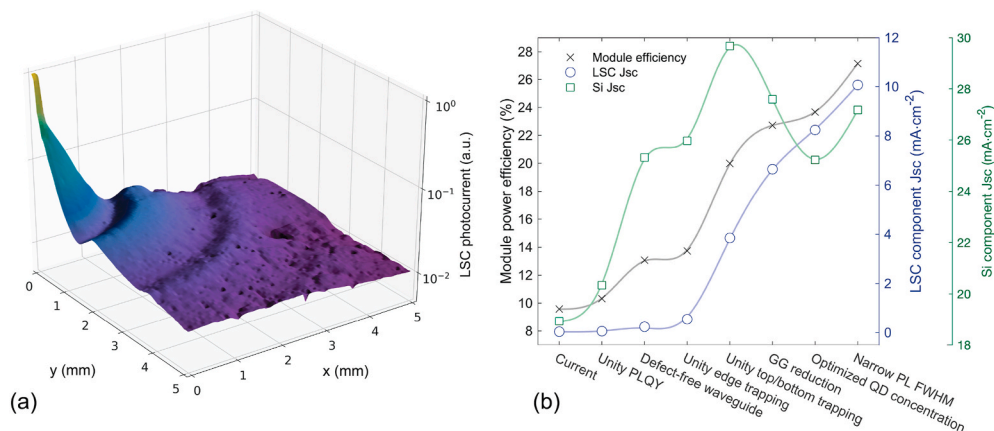

Fig. 7. (a) The photocurrent mapping of a single InGaP micro-cell embedded within a 30 μm waveguide doped with CdSe/CdS QDs plotted on a log scale. A 490 nm laser source scans x- and y-distances up to 5 mm from the outside corner of the device active area (the origin corresponding to the cell center). (b) A performance forecast for the tandem LSC/Si module, illustrating approaches for increased module power efficiency (left y-axis, black x-markers) through optimization of the LSC component, alongside the predicted LSC photocurrent (right y-axis, blue circle-markers) and predicted Si subcell photocurrent (far right y-axis, green square-markers). Efficiencies are modeled for 100% DNI under standard AM1.5G conditions. (For interpretation of the references to colour in this figure legend, the reader is referred to the Web version of this article.)

from reaching the Si component; *vi)* a re-optimized concentration (i.e., optical density) of the QDs within the waveguide (from 0.33 to 2.4 at 450 nm); and *vii)* a decreased QD PL full-width at half-maximum emission profile [48]. As shown, waveguide defects (e.g., PL scattering) marginally affect the LSC performance as a detriment, which is consistent with previous literature on scattering within CdSe/CdS luminophore matrices [27]. By optimizing for each of these components, the tandem device is expected to achieve an ultimate output photocurrent of 10.1 mA/cm^2 and $V_{OC} = 1.48$V for the LSC component with 27.2 mA/cm^2 and $V_{OC} = 0.65$V for the Si subcell. These optimizations are predicted to enable a total module power efficiency of 27.2% under 1-sun illumination, matching previous simulated work given the device spectral characteristics [11,38]. Given this design, tandem LSC/Si devices show promise as a high PCE tandem device with sustained performance in highly diffuse settings.

5. Summary and conclusion

We report an LSC/Si tandem module that demonstrates maintained performance under variable diffusivity conditions. Through outdoor testing at NREL (Golden, CO), we measure the effects of diffuse irradiance on performance of each the LSC top-component and Si subcell. In addition, we simulate a tandem LSC using a Monte Carlo ray-tracing model to quantify the various loss mechanisms present in the module design. We finally forecast that a tandem LSC has the potential to achieve up to 27.2% power conversion efficiency— a significant efficiency increase with respect to the baseline 20.6% efficient Si-only cell under 100% direct normal irradiance—while further maintaining performance across varied DNI conditions.

CRediT authorship contribution statement

Megan Phelan: Conceptualization, Methodology, Data collection, Writing - original draft. **David R. Needell:** Conceptualization, Methodology, Data collection, Writing - original draft. **Haley Bauser:** Conceptualization, Methodology, Data collection, Writing - review & editing. **Hanxiao Su:** Methodology, Data collection. **Michael Deceglie:** Data collection. **San Theingi:** Methodology, Data collection. **Brent Koscher:** Methodology, Data collection. **Zach Nett:** Methodology, Data collection. **Colton R. Bukowsky:** Data collection. **Ognjen Ilic:** Methodology, Data collection. **Paul Stradins:** Conceptualization, Methodology. **John Geisz:** Conceptualization, Methodology, Data collection. **Ralph Nuzzo:** Conceptualization, Methodology. **A. Paul Alivisatos:** Conceptualization, Methodology. **Harry A. Atwater:** Conceptualization, Methodology, Writing - review & editing.

Declaration of competing interest

The authors declare that they have no competing interests with respect to this manuscript.

Acknowledgments

Appendix A. Supplementary data

Supplementary data related to this article can be found at https://doi.org/10.1016/j.solmat.2020.110945.

References

[1] B. Herteleer, J. Cappelle, J. Driesen, Quantifying low-light behaviour of photovoltaic modules by identifying their irradiance- dependent efficiency from data sheets, in: 27th European Photovoltaic Solar Energy Conference, 2012, pp. 3714–3719.

[2] M. Donovan, B. Bourne, J. Roche, Efficiency vs. irradiance characterization of PV modules requires angle-of-incidence and spectral corrections, Conf. Rec. IEEE Photovolt. Spec. Conf. (2010) 2301–2305, https://doi.org/10.1109/PVSC.2010.5615838.

[3] J.L. Kafka, M.A. Miller, A climatology of solar irradiance and its controls across the United States: implications for solar panel orientation, Renew. Energy 135 (2019) 897–907, https://doi.org/10.1016/j.renene.2018.12.057.

[4] C.A. Gueymard, Fixed or tracking solar collectors? Helping the decision process with the solar resource enhancement factor, Opt. Model. Meas. Sol. Energy Syst. II 7046 (2008) 70460D, https://doi.org/10.1117/12.795506. September 2008.

[5] W. Shockley, H.J. Queisser, Detailed balance limit of efficiency of p-n junction solar cells, J. Appl. Phys. 32 (3) (1961) 510–519, https://doi.org/10.1063/1.1736034.

[6] M.A. Green, et al., Solar cell efficiency tables (version 50), Prog. Photovoltaics Res. Appl. 25 (7) (2017) 668–676, https://doi.org/10.1002/pip.2909.

[7] M.A. Green, et al., Solar cell efficiency tables (Version 53), Prog. Photovoltaics Res. Appl. 27 (1) (2019) 3–12, https://doi.org/10.1002/pip.3102.

[8] J.S. Ward, et al., Techno-economic analysis of three different substrate removal and reuse strategies for III-V solar cells, Prog. Photovoltaics Res. Appl. 24 (2016) 1284–1292, https://doi.org/10.1002/pip.

[9] P.S.C. Schulze, et al., 25.1% high-efficiency monolithic perovskite silicon tandem solar cell with a high bandgap perovskite absorber, Sol. RRL 4 (7) (2020) 1–10, https://doi.org/10.1002/solr.202000152.

[10] M.G. Debije, P.P.C. Verbunt, Thirty years of luminescent solar concentrator research: solar energy for the built environment, Adv. Energy Mater. 2 (1) (2012) 12–35, https://doi.org/10.1002/aenm.201100554.

[11] D. R. Needell et al., "Design criteria for micro-optical tandem luminescent solar concentrators," IEEE J. Photovoltaics, vol. 8, no. 6, pp. 1560–1567, Nov. 2018, doi: 10.1109/JPHOTOV.2018.2861751.

[12] M. Carrascosa, S. Unamuno, Monte Carlo simulation of the performance of PMMA luminescent solar collectors, Appl. Optic. 22 (20) (1983) 3236–3241.

[13] M.G. Debije, V.A. Rajkumar, Direct versus indirect illumination of a prototype luminescent solar concentrator, Sol. Energy 122 (2015) 334–340, https://doi.org/10.1016/j.solener.2015.08.036.

[14] A.J. Chatten, K.W.J. Barnham, B.F. Buxton, N.J. Ekins-Daukes, M.A. Malik, A new approach to modelling quantum dot concentrators, Sol. Energy Mater. Sol. Cells 75 (3–4) (2003) 363–371, https://doi.org/10.1016/S0927-0248(02)00182-4.

[15] V. Wittwer, W. Stahl, A. Goetzberger, Fluorescent planar concentrators, Sol. Energy Mater. 11 (3) (1984) 187–197, https://doi.org/10.1016/0165-1633(84)90070-4.

[16] E. Yablonovitch, Thermodynamics of the fluorescent planar concentrator, J. Opt. Soc. Am. 70 (11) (1980) 1362–1363, https://doi.org/10.1364/josa.70.001362.

[17] D.K.G. de Boer, Optimizing wavelength-selective filters for luminescent solar concentrators, Sol. Energy 7725 (2010), https://doi.org/10.1117/12.853846, 77250Q-77250Q–9.

[18] R. Connell, C. Pinnell, V.E. Ferry, Designing spectrally-selective mirrors for use in luminescent solar concentrators, J. Optic. 20 (2) (2018), https://doi.org/10.1088/2040-8986/aaa074.

[19] N.D. Bronstein, et al., Quantum Dot Luminescent Concentrator Cavity Exhibiting 30-fold Concentration, " ACS Photonics, 2015, https://doi.org/10.1021/acsphotonics.5b00334, 150821134054007.

[20] J. Kim, D. Inns, K. Fogel, D.K. Sadana, Surface texturing of single-crystalline silicon solar cells using low density SiO 2 films as an anisotropic etch mask, Sol. Energy Mater. Sol. Cells 94 (2010) 2091–2093, https://doi.org/10.1016/j.solmat.2010.06.026.

[21] J. Grandidier, et al., Solar cell efficiency enhancement via light trapping in printable resonant dielectric nanosphere arrays, Phys. Status Solidi Appl. Mater. Sci. 210 (2) (2013) 255–260, https://doi.org/10.1002/pssa.201228690.

[22] R.H. Fan, et al., Broadband antireflection and light-trapping enhancement of plasmonic solar cells, Phys. Rev. B Condens. Matter 87 (19) (2013) 1–7, https://doi.org/10.1103/PhysRevB.87.195444.

[23] J.N. Munday, H.A. Atwater, Large integrated absorption enhancement in plasmonic solar cells by combining metallic gratings and antireflection coatings, Nano Lett. 11 (6) (2011) 2195–2201, https://doi.org/10.1021/nl101875t.

[24] V.E. Ferry, L.A. Sweatlock, D. Pacifici, H.A. Atwater, Plasmonic nanostructure design for efficient light coupling into solar cells vivian, Nano Lett. 8 (12) (2008) 4391–4397.

[25] S.W. Boettcher, et al., Energy-conversion properties of vapor-liquid-solid-grown silicon wire-array photocathodes, Science 84 327 (5962) (2010), https://doi.org/10.1126/science.1180783, 185–7.

[26] M.D. Kelzenberg, et al., Enhanced absorption and carrier collection in Si wire arrays for photovoltaic applications, Nat. Mater. 9 (3) (2010) 239–244, https://doi.org/10.1038/nmat2635.

[27] N.D. Bronstein, et al., Quantum dot luminescent concentrator cavity exhibiting 30-fold concentration, ACS Photonics 2 (11) (2015) 1576–1583, https://doi.org/10.1021/acsphotonics.5b00334.

[28] H.-J. Song, B.G. Jeong, J. Lim, D.C. Lee, W.K. Bae, V.I. Klimov, Performance limits of luminescent solar concentrators tested with seed/quantum-well quantum dots in a selective-reflector-based optical cavity, Nano Lett. 18 (1) (Jan. 2018) 395–404, https://doi.org/10.1021/acs.nanolett.7b04263.

[29] N.D. Bronstein, et al., Luminescent solar concentration with semiconductor nanorods and transfer-printed micro-silicon solar cells, ACS Nano 8 (1) (Jan. 2014) 44–53, https://doi.org/10.1021/nn404418h.

[30] X. Sheng, et al., Doubling the power output of bifacial thin-film GaAs solar cells by embedding them in luminescent waveguides, Adv. Energy Mater. 3 (8) (Aug. 2013) 991–996, https://doi.org/10.1002/aenm.201201064.

[31] S. Essig, et al., Raising the one-sun conversion efficiency of III-V/Si solar cells to 32.8% for two junctions and 35.9% for three junctions, Nat. Energy 2 (9) (2017), https://doi.org/10.1038/nenergy.2017.144.

[32] J.F. Geisz, et al., Enhanced external radiative efficiency for 20.8% efficient single-junction GaInP solar cells, Appl. Phys. Lett. 103 (4) (2013), https://doi.org/10.1063/1.4816837.

[33] C. Dagdeviren, et al., Thin film receiver materials for deterministic assembly by transfer printing, Chem. Mater. 26 (11) (2014) 3502–3507, https://doi.org/10.1021/cm501002b.

[34] A. Carlson, A.M. Bowen, Y. Huang, R.G. Nuzzo, J.A. Rogers, Transfer printing techniques for materials assembly and micro/nanodevice fabrication, Adv. Mater. 24 (39) (2012) 5284–5318, https://doi.org/10.1002/adma.201201386.

[35] R. Nuzzo, I.L. Us, E. Menard, N.C. Us, Optical systems fabricated by printing-based assembly, US Pat. 2 (12) (2015).

[36] D.L. Young, et al., Low-cost plasma immersion ion implantation doping for Interdigitated back passivated contact (IBPC) solar cells, Sol. Energy Mater. Sol. Cells 158 (2016) 68–76, https://doi.org/10.1016/j.solmat.2016.05.044.

[37] T.S. Parel, C. Pistolas, L. Danos, T. Markvart, Modelling and experimental analysis of the angular distribution of the emitted light from the edge of luminescent solar concentrators, Opt. Mater. 42 (2015), https://doi.org/10.1016/j.optmat.2015.02.011.

[38] D. R. Needell, C. R. Bukowsky, S. Darbe, H. Bauser, O. Ilic, and H. A. Atwater, "Spectrally matched quantum dot photoluminescence in GaAs-Si tandem luminescent solar concentrators," IEEE J. Photovoltaics, vol. 9, no. 2, pp. 397–401, Mar. 2019, doi: 10.1109/JPHOTOV.2019.2892075.

[39] I.M. Slauch, M.G. Deceglie, T.J. Silverman, V.E. Ferry, et al., Outdoor Testing of c-Si Photovoltaic Modules with Spectrally-Selective Mirrors for Operating Temperature Reduction, 46th IEEE Photovolt. Spec. Conf. (2019) 112–117, https://doi.org/10.1109/PVSC40753.2019.8981160.

[40] R. An, et al., Photostability and photodegradation processes in colloidal CsPbI3 perovskite quantum dots, ACS Appl. Mater. Interfaces 10 (45) (2018) 39222–39227, https://doi.org/10.1021/acsami.8b14480.

[41] T. Aubert, et al., Bright and stable CdSe/CdS@SiO2nanoparticles suitable for long-term cell labeling, ACS Appl. Mater. Interfaces 6 (14) (2014) 11714–11723, https://doi.org/10.1021/am502367b.

[42] E.F. Fernández, F. Almonacid, P.M. Rodrigo, P.J. Pérez-Higueras, CPV systems, in: McEvoy's Handbook Of Photovoltaics: Fundamentals and Applications, Elsevier Inc., 2018, pp. 931–985.

[43] W.G.J.H.M. Van Sark, Z. Krumer, C.D.M. Donegá, R.E.I. Schropp, "Luminescent solar Concentrators : the route to 10 % efficiency, IEEE J. Photovoltaics, 2014, pp. 2276–2279.

[44] D. Fleischman, K.T. Fountaine, C.R. Bukowsky, G. Tagliabue, L.A. Sweatlock, H.A. Atwater, High spectral resolution plasmonic color filters with subwavelength dimensions, ACS Photonics 6 (2019) 332–338, https://doi.org/10.1021/acsphotonics.8b01634.

[45] H.Y. Kim, D.E. Yoon, J. Jang, G.M. Choi, D.C. Lee, B.S. Bae, Quantum dot/siloxane composite film exceptionally stable against heat and moisture, Dig. Tech. Pap. - SID Int. Symp. 48 (1) (2017) 452–454, https://doi.org/10.1021/jacs.6b10681.

[46] V.I. Klimov, T.A. Baker, J. Lim, K.A. Velizhanin, H. McDaniel, Quality factor of luminescent solar concentrators and practical concentration limits attainable with semiconductor quantum dots, ACS Photonics 3 (6) (2016) 1138–1148, https://doi.org/10.1021/acsphotonics.6b00307.

[47] Y.J. Choi, D. Hwang, H. Chung, D.Y. Kim, D.Y. Kim, Controlling the spatial distribution of quantum dots in nanofiber for light-harvesting devices, NPG Asia Mater. 7 (7) (Jul. 2015) e202–e207, https://doi.org/10.1038/am.2015.76.

[48] O. Chen, et al., Compact high-quality CdSe-CdS core-shell nanocrystals with narrow emission linewidths and suppressed blinking, Nat. Mater. 12 (5) (2013) 445–451, https://doi.org/10.1038/nmat3539.